Single-Atom Catalysis Hot Paper

Deutsche Ausgabe: DOI: 10.1002/ange.201604802
Internationale Ausgabe: DOI: 10.1002/anie.201604802

# Single Cobalt Atoms with Precise N-Coordination as Superior Oxygen Reduction Reaction Catalysts

*Peiqun Yin, Tao Yao, Yuen Wu,* Lirong Zheng, Yue Lin, Wei Liu, Huanxin Ju, Junfa Zhu, Xun Hong, Zhaoxiang Deng, Gang Zhou, Shiqiang Wei, and Yadong Li**

***Abstract:*** *A new strategy for achieving stable Co single atoms (SAs) on nitrogen-doped porous carbon with high metal loading over 4 wt% is reported. The strategy is based on a pyrolysis process of predesigned bimetallic Zn/Co metal–organic frameworks, during which Co can be reduced by carbonization of the organic linker and Zn is selectively evaporated away at high temperatures above 800 °C. The spherical aberration correction electron microscopy and extended X-ray absorption fine structure measurements both confirm the atomic dispersion of Co atoms stabilized by as-generated N-doped porous carbon. Surprisingly, the obtained Co-$N_x$ single sites exhibit superior ORR performance with a half-wave potential (0.881 V) that is more positive than commercial Pt/C (0.811 V) and most reported non-precious metal catalysts. Durability tests revealed that the Co single atoms exhibit outstanding chemical stability during electrocatalysis and thermal stability that resists sintering at 900 °C. Our findings open up a new routine for general and practical synthesis of a variety of materials bearing single atoms, which could facilitate new discoveries at the atomic scale in condensed materials.*

Nanomaterials exhibit unexpected properties when they are downsized to atomic scale.[1] Investigating the properties of single atoms is fundamentally important but remains challenging in condensed physics and materials science because of the difficulties associated with preparation. To obtain metal SA catalysts, the generation of atomically dispersed metal atoms can be achieved either by physical[2] or chemical methods.[3] The stabilization of metal SAs is mostly based on a bottom-up strategy, during which the metal precursor are adsorbed, reduced, and confined by the defect-rich support.[4] Though much effort has been invested, this emerging area is still characterized by significant challenges. First, to fully deposit the well-defined single-metal atoms on the surface of an incorporated support, the concentration of metal atoms should be extremely low to avoid aggregation.[5] Thus far, the requirement of practical and high yield (>1 wt% metal) synthesis of metal SA catalysts has been challenging to satisfy, and the low loading of metal SAs on supported catalysts hinders further study of their macroscopic properties. Second, in most cases the architectural structures of anchor sites for confinement and stabilization of metal SAs on a support remain elusive, and consequently, the coordination environment for metal SAs are inhomogeneous and are poorly defined. In this regard, the precise structure of metal SAs, such as coordination number, dispersion tendencies, and binding mode are difficult to identify and control, delaying the advancement of SA catalysts.

Metal-supported N-doped carbon materials are becoming one of the most promising candidates to replace Pt-based catalysts, in acidic or alkaline medium.[6] As is well-known, metal–organic frameworks (MOFs) are composed of metal-containing nodes and organic linkers, which are typically characterized by atomically dispersed metal sites.[7] Pyrolysis of MOFs or ZIFs serves as an important route to metal-supported N-doped carbon materials.[8] However, there are few studies reporting methods for generation of single metal atom-reactive sites because of the drastic reactive processes that occur at high temperature. Metals residing in MOF/ZIF nodes may be partly exchanged with other metals because of the coordination environment provided by the MOF/ZIF linkers, allowing further adjustment of the spatial distance of metal sites. If we can selectively remove the doping metal and reduce the remaining metal in situ, supported metal SAs (or cluster structures) distributed on porous matrices may be fabricated.

Accounting for the same sodalite coordination of $Co^{2+}$ and $Zn^{2+}$ with 2-methylimidazole,[9] a type of Zn/Co bimetallic MOF (BMOF) with a homogeneous distribution of Zn and Co can be systematically designed (Supporting Information, Figures S1 and S2).[10] The intentional addition of $Zn^{2+}$ can replace a certain proportion of $Co^{2+}$ sites and serve as a "fence" to further expand the adjacent distances of Co atoms. The low boiling point Zn atoms (mp 420 °C, bp 907 °C) can be evaporated away at high temperatures over 800 °C, and

[*] P. Yin, Prof. Y. Wu, X. Hong, Prof. Y. Li
Department of Chemistry and Center of Advanced Nanocatalysis (CAN-USTC) University of Science and Technology of China
Hefei, Anhui 230026 (China)
and
Department of Chemistry and Collaborative Innovation Center for Nanomaterial Science and Engineering, Tsinghua University
Beijing 100084 (China)
E-mail: yuenwu@ustc.edu.cn
ydli@mail.tsinghua.edu.cn
T. Yao, Y. Lin, W. Liu, H. Ju, J. Zhu, S. Wei
Hefei National Laboratory for Physical Sciences at the Microscale
University of Science and Technology of China
Hefei, Anhui Province 230026 (China)
G. Zhou
State Key Laboratory of Chemical Resource Engineering
Beijing University of Chemical Technology
Beijing 100029 (China)
L. Zheng
Institute of High Energy Physics
Beijing 100029 (China)

Supporting information for this article can be found under: http://dx.doi.org/10.1002/anie.201604802.

  

Co nodes are reduced in situ by carbonization of the organic linker. Since the molar ratio of Zn/Co added is elevated above 1:1, Co single atoms/nitrogen-doped porous carbon (Co SAs/*N*-C) can be successfully synthesized. The structural adjustability of MOFs also endows the possibility to generalize this strategy to other metal SA materials if the precursors are built up strategically. Moreover, control over the spatial dispersion, metal loading, and coordination structure of SAs can be achieved by this disassembly strategy.

The transmission electron microscopy (TEM) image in Figure 1 a and high-angle annular dark-field scanning transmission electron microscope (HAADF-STEM) image in Figure 1 b both reveal that the as-prepared Co SAs/*N*-C structure retains the initial rhombododecahedral shape and size of the starting $Zn_1Co_1$-BMOF (Zn/Co = 1:1) material. The ring-like selected area electron diffraction (SAED) pattern taken from an individual rhombododecahedron demonstrated its poor crystallinity (Figure 1 c). To elucidate the form of the Co atoms, we carried out aberration corrected HAADF-STEM measurements (Figure 1 d,e) with sub-angstrom resolution; contrast is characteristic of atomic number.[11] The isolated heavier Co SAs could be discerned in the carbon support because of a different Z-contrast between Co and C. Careful examinations of different areas confirmed the absence of Co cluster and small crystals (Supporting Information, Figure S3). Figure 1 f shows the representative Co, N, and C mappings of Co SAs/*N*-C by electron energy-loss spectroscopy (EELS). N-mapping indicates that the N heteroatom is homogenously distributed over the entire architecture, resulting from the decomposition of N-containing linkers. To localize the spatial distribution of Co SAs, a series of HAADF-STEM images with different focal depths were measured. The three selected atoms ($a_1$, $b_1$, and $c_1$) in the summed through-focal HAADF images (Figure 1 g) should show different intensities at specific focal depths; these were analyzed to determine the relative vertical positions along the electron beam direction.[12] As shown in the intensity versus defocus function (Figure 1 h), the $c_1$ atom situated between $a_1$ and $b_1$ along the *x*-axis is lowest at a focal position along the *z*-axis. Therefore, it is believed that the Co SAs distribute in a highly dispersed fashion on N-doped carbon in three dimensions, and not only on the surface.

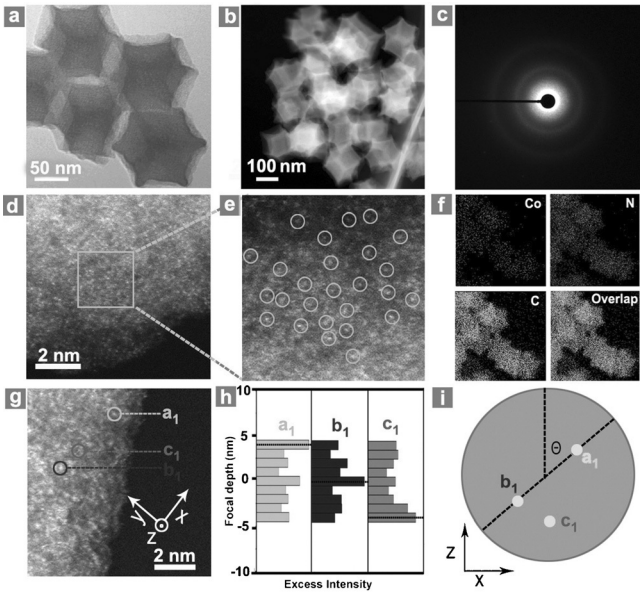


***Figure 1.*** a) TEM and b) HAADF-STEM images of Co SAs/*N*-C(800). c) Corresponding SAED pattern of an individual rhombododecahedron of Co SAs/*N*-C(800). d, e) Magnified HAADF-STEM images of Co SAs/*N*-C(800), showing that only Co single atoms are present in Co SAs/*N*-C. f) Examination of the corresponding EELS mapping reveals the homogeneous distribution of Co and N on the carbon support. g–i) Three-dimensional dispersions of Co atoms on Co SAs/*N*-C(800). (g) Sum of nine aligned HAADF-STEM images of Co SAs/*N*-C(800). h) Excess intensity of atoms a1, b1, c1 indicated in (g). i) The spatial locations of atoms a1, b1, and c1 along the *x*- and *z*-axis, respectively.

Indeed, the addition of Zn plays a pivotal role in the formation of Co SAs. On one hand, the spatial interval between two Co atoms can be finely controlled. On the other hand, the leaving $Zn^{2+}$ sites generate free N sites during pyrolysis, which are beneficial for the stabilization of Co SAs. As shown in Figure S4 (Supporting Information), the pure Co-containing MOF (ZIF-67) only resulted in Co nanoparticles (NPs) without the protection of Zn. This result was also confirmed by the X-ray diffraction (XRD) patterns (Supporting Information, Figure S5); a set of well-defined face-centered cubic Co peaks appear for pyrolyzed ZIF-67. In contrast, utilizing $Zn_1Co_1$-BMOF as a precursor, no peaks characteristic of Co crystals emerged even when the temperature was raised to 900 °C (Figure 2 a). The sample at 900 °C retained atomic dispersion of Co atoms, as supported by the aberration corrected HAADF-STEM observation in Figure S6 (Supporting Information) and denoted as Co SAs/*N*-C(900). When the temperature was raised to 1000 °C, the crystallized Co phase prevailed, as confirmed by the appearance of Co NPs (Supporting Information, Figure S7). Under similar pyrolysis conditions, increasing Zn/Co ratio did not give rise to the aggregation of Co atoms, but a decreased Zn/Co ratio (0.75:1) was not able to offer sufficient confinement and resulted in the formation of Co–Co bonds (Supporting Information, Figure S8).

X-ray photoelectron spectroscopy (XPS) measurements revealed that the Co atoms of BMOFs are in a cationic environment with a high binding energy of Co $2p_{1/2}$ at 780.7 eV (Supporting Information, Figure S9). For the pyrolysis of ZIF-67, the Co $2p_{1/2}$ signals down-shifted to 778.8 eV and finally exhibited a metallic state corresponding to the reduction process. A similar down-shift of Co 2p was also observed for $Zn_1Co_1$-BMOF, but the valence states of the resulting Co SAs were characterized by a slight positive charge because of N-coordination.[13] The high-resolution XPS spectrum for N 1s revealed that the dominant nitrogen species after pyrolysis are pyridinic-N and graphitic-N (Supporting Information, Figure S10), which serve as anchor points for Co SAs. The proportion of these two N species decreased significantly when the pyrolysis temperature increased from 800 °C to 900 °C, indicating that some coordination bonds between N and Co atoms were broken. At 900 °C the evaporation of Zn was tracked by 1) disappearance of the Zn XPS signals (Supporting Information,

  

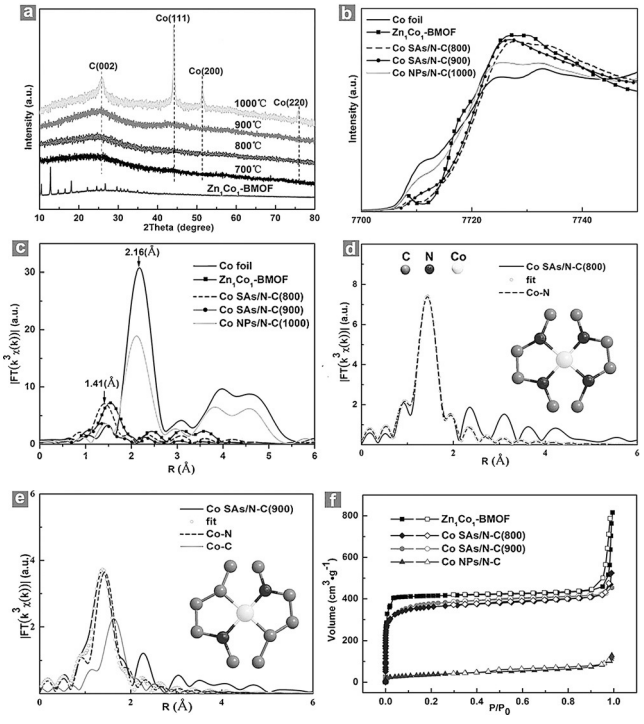


***Figure 2.*** a) The XRD of the as-prepared samples by annealing of $Zn_1Co_1$-BMOF at different temperatures. b) Co K-edge XANES spectra and c) the k3-weighted χ(k)-function of the EXAFS spectra. The corresponding EXAFS fitting curves for the samples d) Co SAs/*N*-C(800) and e) Co SAs/*N*-C(900). Insets are the proposed Co-$N_x$ architectures. f) $N_2$ adsorption and desorption isotherms for $Zn_1Co_1$-BMOF, Co SAs/*N*-C, and Co NPs/*N*-C.

Figure S11) and 2) decreasing Zn/Co ratios with respect to pyrolysis time (Supporting Information, Figure S12).

X-ray absorption fine structure (XAFS) measurements were performed to verify that the isolated dispersed Co SAs are the only form of Co present, and to clarify how they are stabilized. As shown in the X-ray absorption near-edge structure (XANES) spectra (Figure 2b), the position of the white line peak for Co SAs/*N*-C(800) and Co SAs/*N*-C(900) is located between those of Co foil and $Zn_1Co_1$-BMOF precursor, indicating that the valence state of Co SAs is situated between that of $Co^0$ and $Co^{II}$. This observation agrees well with the aforementioned XPS results and reported density functional theory (DFT) predictions, which suggest that single Co sites possess a porphyrinic planar structure.[14] By contrast, the XANES spectrum of Co NPs/*N*-C(1000) was closer to that of Co foil, which reveals the dominance of $Co^0$ NPs at 1000 °C.

Further structural information about Co atoms can be obtained from the extended X-ray absorption fine structure (EXAFS). The Fourier transforms (*r* space; Supporting Information, Figure S13) for ZIF-67 and $Zn_1Co_1$-BMOF exhibited similar Co–N coordination with a peak at 1.60 Å, which is ascribed to tetrahedral coordination of Co atoms in a sodalite crystal form. After pyrolysis, the Co–N coordination peak shifts to a low R-position for the Co SAs/*N*-C(800) at 1.41 Å, demonstrating that the main coordination mode of Co varies slightly (Figure 2c). Importantly, the Fourier transform curves for Co SAs/*N*-C(800) and Co SAs/*N*-C(900) clearly indicate that the Co atoms are atomically dispersed; Co–Co paths at 2.16 Å are absent. Furthermore, according to the fitting parameters given in Table S1 (Supporting Information), the coordination numbers of Co–N within Co SAs/*N*-C(800) and Co SAs/*N*-C(900) are 4 and 2, respectively. That is, a certain amount of Co–N coordination bonds were broken by increasing the pyrolysis temperature (a decreased N:Co ratio is observed with increasing temperature; Supporting Information, Table S2). In other words, the dominant reactive sites for Co SAs/*N*-C obtained at 800 and 900 °C can be postulated as planar Co-$N_4$ and Co-$N_2$, respectively (Figure 2d,e). This result also explains why Co SAs with such high metal concentration can be stabilized on this highly porous structure. The appearance of a Co–Co coordination peak for Co NPs/*N*-C(1000) indicates that a temperature as high as 1000 °C breaks the Co–N bonds and causes the formation of Co NPs (Supporting Information, Figure S13). The supplementary EXAFS results for the pyrolysis of ZIF-67, $Zn_{1.25}Co_1$, and $Zn_{0.75}Co_1$ BMOFs reinforce the pivotal role of Zn dopant in Co SAs/*N*-C (Supporting Information, Figure S14).

Base on the above results, a mechanism illustrating the formation process of Co SAs/*N*-C is summarized in Figure 3. During the annealing treatment under a $N_2$ environment, the organic linkers of MOFs undergo a pyrolysis process to generate N-doped porous carbon.[15] Subsequently, the metal nodes are reduced at high temperature by the generated carbon. Pre-meditated mixing of Zn can vary the distance of adjacent Co atoms and provide more free N sites, preventing the formation of Co–Co bonds at high temperature. After the evaporation of low boiling point Zn atoms, the remaining Co atoms anchor on the N-doped carbon support.

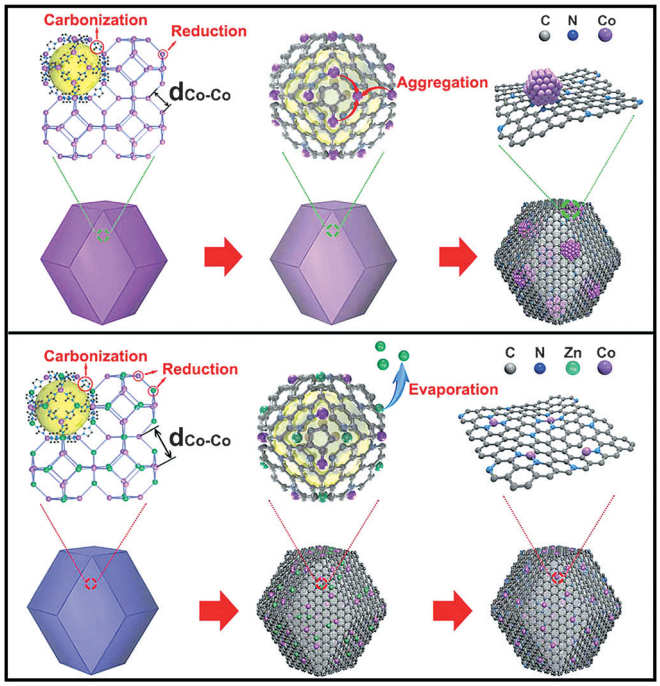


***Figure 3.*** The formation of Co NPs-N/C (top) and Co SAs/*N*-C (bottom).

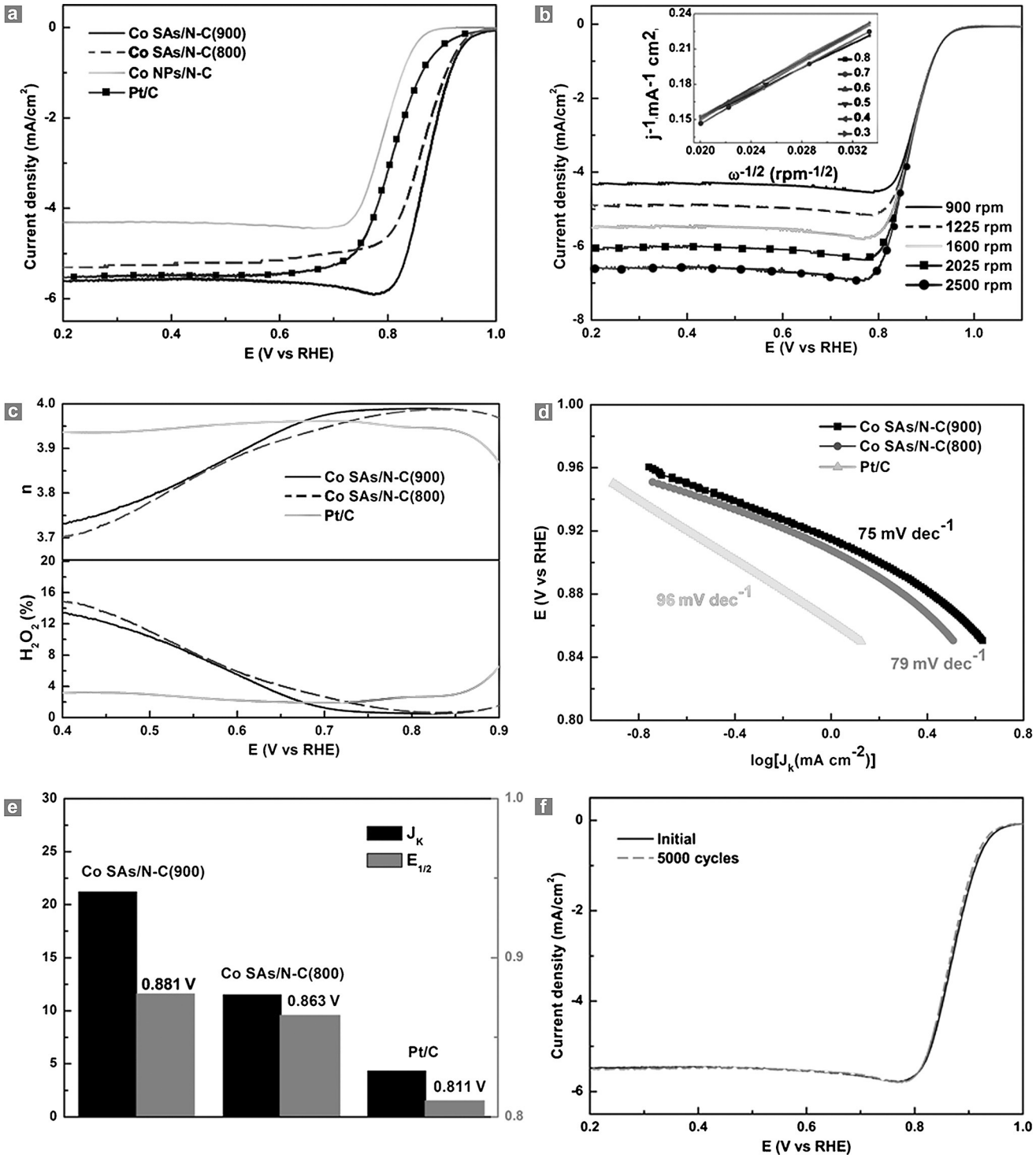


***Figure 4.*** a) RDE polarization curves of Co SAs/*N*-C, Co NPs-N/C, and Pt/C in $O_2$-saturated 0.1 M KOH with a sweep rate of 10 mV/S and 1600 rpm. b) RDE polarization curves of Co SAs/*N*-C(900) at different rotation rates. c) Electron transfer number (*n*; top) and $H_2O_2$ yield (bottom) vs. potential. d) Corresponding Tafel plots obtained from the RDE polarization curves. e) Comparison of $E_{1/2}$ and $J_k$ for different catalysts. f) LSV curves of Co SAs before and after 5000 potential cycles in $O_2$-saturated 0.1 M KOH.

Analysis of Brunauer–Emmett–Teller (BET) adsorption–desorption isotherms indicate that Co SAs/*N*-C maintain a highly open surface area and porous structure (Figure 3 f; Supporting Information, Table S3). These features frame the Co SAs/*N*-C as an ideal catalyst for the oxygen reduction reaction (ORR), which is paramount for metal–air batteries and fuel cells.[13a,16] The ORR test was studied by steady-state linear sweep voltammetry (LSV) on a rotating disk electrode (RDE) in $O_2$-saturated 0.1M KOH. For better comparison, we prepared N-doped carbon catalyst by the pyrolysis of ZIF-8

  

(pure Zn-containing MOF) to evaluate the activity of N dopants in a carbon lattice. However, as shown in Figure S16 (Supporting Information), this as-prepared C-N material exhibited very poor activity in the ORR, indicating that the activity of Co SAs/*N*-C catalysts can largely be ascribed to metal-*N*-C sites rather than C-N sites. When compared to Co NPs/*N*-C and commercial Pt/C catalysts, the best ORR activity was achieved by Co SAs/*N*-C(900), as judged by the onset ($E_{onset}$) and half-wave ($E_{1/2}$) potentials in Figure 4a. The $E_{onset}$ of Co SAs/*N*-C(900) was almost the same as that of Pt/C (0.982 V vs. RHE), while its $E_{1/2}$ (0.881 V) was more positive than those of Pt/C (0.811 V) and Co SAs/*N*-C(800) (0.863 V), and also surpassed that of most non-precious metal catalysts reported (Supporting Information, Table S4). This result coincided well with our DFT prediction that Co-$N_2$ species show a stronger interaction with peroxide than Co-$N_4$ (which are dominant in Co SAs/*N*-C(800)), and promoted the four-electron reduction process of the ORR (see details in the Supporting Information). The Koutecky–Levich (K-L) plots for Co SAs/*N*-C(900), obtained from RDE polarization curves at different rotating speeds (Figure 4b), presented nearly parallel fitting lines, suggesting first-order reaction kinetics with respect to $O_2$ concentration and a potential-independent electron transfer rate. The high electron transfer rate was confirmed by the rotating ring disk electrode (RRDE) tests (Figure 4c), demonstrating a near four-electron ORR pathway over the single Co-$N_2$ sites.[17] The kinetic current density ($J_k$) at 0.8 V, derived from the intercept of K-L plots and small Tafel slope of 75 mV $dec^{-1}$ (Figure 4d), further verified the superior activity of Co SAs/*N*-C(900) (Figure 4e). Strikingly, there is no obvious decay in $E_{1/2}$ after 5000 continuous potential cycles (Figure 4f), demonstrating that the Co SAs/*N*-C(900) catalyst also exhibits excellent durability. Careful examination of many HAADF images (Supporting Information, Figure S17) confirmed that the atomically isolated Co atoms were retained after durability tests, which further underlines the stability of the material.

In summary, a general strategy enabling the practical and controlled synthesis of supported metal SA catalysts with atomic dispersion, high metal loading, and excellent molecular accessibility, has been developed and applied to a series of metal SAs/*N*-C. The stabilization of Co SAs is strictly related to the N-doped porous carbon support, which is derived from pyrolysis of MOFs and the mixing of Zn as a "fence" to expand the distance of adjacent Co atoms in space. This finding may open up a new family of single-metal or single-molecule materials, which show great potential in condensed science as a result of their properties.

## Acknowledgements

This work was supported by the Fundamental Research Funds for the Central Universities (WK2060190043), National Natural Science Foundation of China (U1463202 and 21522107), State Key Project of Fundamental Research for Nanoscience and Nanotechnology (2011CB932401 and 2011CBA00500), National key Basic Research Program of China (2012CB224802).

**Keywords:** coordination control · metal single atoms · metal–organic frameworks · oxygen reduction reaction

**How to cite:** *Angew. Chem. Int. Ed.* **2016**, *55*, 10800–10805
*Angew. Chem.* **2016**, *128*, 10958–10963

[1] a) H. Fei, J. Dong, M. J. Arellano-Jiménez, G. Ye, N. D. Kim, E. L. Samuel, Z. Peng, Z. Zhu, F. Qin, J. Bao, et al., *Nat. Commun.* **2015**, *6*, 8668; b) B. Qiao, J.-X. Liang, A. Wang, C.-Q. Xu, J. Li, T. Zhang, J. Liu, *Nano Res.* **2015**, *8*, 2913–2924.

[2] a) K. Judai, S. Abbet, A. S. Wörz, U. Heiz, C. R. Henry, *J. Am. Chem. Soc.* **2004**, *126*, 2732–2737; b) S. Lee, C. Fan, T. Wu, S. L. Anderson, *J. Am. Chem. Soc.* **2004**, *126*, 5682–5683; c) Y. Lei, F. Mehmood, S. Lee, J. Greeley, B. Lee, S. Seifert, R. E. Winans, J. W. Elam, R. J. Meyer, P. C. Redfern, *Science* **2010**, *328*, 224–228; d) H. Yan, H. Cheng, H. Yi, Y. Lin, T. Yao, C. Wang, J. Li, S. Wei, J. Lu, *J. Am. Chem. Soc.* **2015**, *137*, 10484–10487.

[3] B. Qiao, A. Wang, X. Yang, L. F. Allard, Z. Jiang, Y. Cui, J. Liu, J. Li, T. Zhang, *Nat. Chem.* **2011**, *3*, 634–641.

[4] a) X. Guo, G. Fang, G. Li, H. Ma, H. Fan, L. Yu, C. Ma, X. Wu, D. Deng, M. Wei, *Science* **2014**, *344*, 616–619; b) S. Sun, G. Zhang, N. Gauquelin, N. Chen, J. Zhou, S. Yang, W. Chen, X. Meng, D. Geng, M. N. Banis, et al., *Sci. Rep.* **2013**, *3*, 1775; c) G. Kyriakou, M. B. Boucher, A. D. Jewell, E. A. Lewis, T. J. Lawton, A. E. Baber, H. L. Tierney, M. Flytzani-Stephanopoulos, E. H. Sykes, *Science* **2012**, *335*, 1209–1212.

[5] a) K. Ding, A. Gulec, A. M. Johnson, N. M. Schweitzer, G. D. Stucky, L. D. Marks, P. C. Stair, *Science* **2015**, *350*, 189–192; b) H. Zhang, T. Watanabe, M. Okumura, M. Haruta, N. Toshima, *Nat. Mater.* **2012**, *11*, 49–52; c) S. Zhang, L. Nguyen, J.-X. Liang, J. Shan, J. Liu, A. I. Frenkel, A. Patlolla, W. Huang, J. Li, F. Tao, *Nat. Commun.* **2015**, *6*, 7938; d) G. Vilé, D. Albani, M. Nachtegaal, Z. Chen, D. Dontsova, M. Antonietti, N. López, J. Pérez-Ramírez, *Angew. Chem. Int. Ed.* **2015**, *54*, 11265–11269; *Angew. Chem.* **2015**, *127*, 11417–11422.

[6] a) G. Wu, K. L. More, C. M. Johnston, P. Zelenay, *Science* **2011**, *332*, 443–447; b) H.-x. Zhong, J. Wang, Y.-w. Zhang, W.-l. Xu, W. Xing, D. Xu, Y.-f. Zhang, X.-b. Zhang, *Angew. Chem. Int. Ed.* **2014**, *53*, 14235–14239; *Angew. Chem.* **2014**, *126*, 14459–14463; c) T. Y. Ma, S. Dai, M. Jaroniec, S. Z. Qiao, *J. Am. Chem. Soc.* **2014**, *136*, 13925–13931; d) W. Zhang, Z.-Y. Wu, H.-L. Jiang, S.-H. Yu, *J. Am. Chem. Soc.* **2014**, *136*, 14385–14388.

[7] a) S. Kitagawa, *Chem. Soc. Rev.* **2014**, *43*, 5415–5418; b) H.-C. Zhou, J. R. Long, O. M. Yaghi, *Chem. Rev.* **2012**, *112*, 673–674; c) A. Corma, H. Garcia, F. X. L. i. Xamena, *Chem. Rev.* **2010**, *110*, 4606–4655.

[8] a) Y. Z. Chen, C. Wang, Z. Y. Wu, Y. Xiong, Q. Xu, S. H. Yu, H. L. Jiang, *Adv. Mater.* **2015**, *27*, 5010–5016; b) M. Zhou, H.-L. Wang, S. Guo, *Chem. Soc. Rev.* **2016**, *45*, 1273–1307; c) B. You, N. Jiang, M. Sheng, W. S. Drisdell, J. Yano, Y. Sun, *Acs Catal.* **2015**, *5*, 7068–7076.

[9] a) K. S. Park, Z. Ni, A. P. Côté, J. Y. Choi, R. Huang, F. J. Uribe-Romo, H. K. Chae, M. O'Keeffe, O. M. Yaghi, *Proc. Natl. Acad. Sci. USA* **2006**, *103*, 10186–10191; b) X. C. Huang, Y. Y. Lin, J. P. Zhang, X. M. Chen, *Angew. Chem.* **2006**, *118*, 1587–1589; c) R. Banerjee, A. Phan, B. Wang, C. Knobler, H. Furukawa, M. O'Keeffe, O. M. Yaghi, *Science* **2008**, *319*, 939–943.

[10] J. Yang, F. Zhang, H. Lu, X. Hong, H. Jiang, Y. Wu, Y. Li, *Angew. Chem. Int. Ed.* **2015**, *54*, 10889–10893; *Angew. Chem.* **2015**, *127*, 11039–11043.

[11] a) S. Pennycook, *Ultramicroscopy* **1989**, *30*, 58–69; b) P. Midgley, M. Weyland, *Ultramicroscopy* **2003**, *96*, 413–431.

[12] J. E. Allen, E. R. Hemesath, D. E. Perea, J. L. Lensch-Falk, Z. Li, F. Yin, M. H. Gass, P. Wang, A. L. Bleloch, R. E. Palmer, *Nat. Nanotechnol.* **2008**, *3*, 168–173.

[13] a) M. Lefèvre, E. Proietti, F. Jaouen, J.-P. Dodelet, *Science* **2009**, *324*, 71–74; b) J. Herranz, F. Jaouen, M. Lefevre, U. I. Kramm,

  

E. Proietti, J.-P. Dodelet, P. Bogdanoff, S. Fiechter, I. Abs-Wurmbach, P. Bertrand, *J. Phys. Chem. C* **2011**, *115*, 16087 – 16097.
[14] a) A. Zitolo, V. Goellner, V. Armel, M.-T. Sougrati, T. Mineva, L. Stievano, E. Fonda, F. Jaouen, *Nat. Mater.* **2015**, *14*, 937 – 942; b) S. Kattel, P. Atanassov, B. Kiefer, *J. Mater. Chem. A* **2014**, *2*, 10273 – 10279.
[15] B. Liu, H. Shioyama, T. Akita, Q. Xu, *J. Am. Chem. Soc.* **2008**, *130*, 5390 – 5391.
[16] a) Z. Chen, D. Higgins, A. Yu, L. Zhang, J. Zhang, *Energy Environ. Sci.* **2011**, *4*, 3167 – 3192; b) C. Chen, Y. Kang, Z. Huo, Z. Zhu, W. Huang, H. L. Xin, J. D. Snyder, D. Li, J. A. Herron, M. Mavrikakis, *Science* **2014**, *343*, 1339 – 1343.
[17] S. Guo, S. Zhang, S. Sun, *Angew. Chem. Int. Ed.* **2013**, *52*, 8526 – 8544; *Angew. Chem.* **2013**, *125*, 8686 – 8705.

Received: May 17, 2016
Revised: June 22, 2016
Published online: August 4, 2016

  